Fast high-quality numerical shadowing of chaotic maps using synchronization

Mitrajit Dutta*
Department of Mathematics and Statistics, University of New Hampshire, Durham, New Hampshire 03824, USA
(Received 31 May 2005; revised manuscript received 3 October 2005; published 22 November 2005)

For a chaotic, dynamical system, a typical noisy trajectory diverges exponentially from the true trajectory with the same initial conditions. Nonetheless, the noisy trajectory, as representative of the dynamical system, may have credibility if there exists a true trajectory, corresponding to a slightly different initial condition, that stays close to the noisy trajectory for long periods of time. For finding such shadowing trajectories, a synchronization based method is presented. We call it the *synchronize-and-pullback* algorithm. Several numerical examples are shown illustrating the method. Finally, an application of the proposed shadowing technique for noise filtration in the context of communication is presented.

DOI: 10.1103/PhysRevE.72.056214 PACS number(s): 05.45.Pq, 05.45.Xt, 05.45.Vx

I. INTRODUCTION

A wide class of physical systems of interest may be described by deterministic, dynamical systems. Although the equations describing the evolution of these dynamical systems may be available, often these equations cannot be solved analytically. Under such circumstances, one must resort to numerical means in order to generate the trajectories and study them. Such computer generated numerical trajectories are never exact since errors due to discretization and finite-precision arithmetic are introduced at every step of iteration. However, if these errors are kept small, then it may be reasonable to expect the error in the final solution to be small as well. Thus as long as the errors at every step remain adequately small, the computer generated numerical trajectories may be acceptable.

Unfortunately, the situation deteriorates dramatically when the dynamical system of interest happens to be chaotic. Trajectories corresponding to chaotic, dynamical systems, although bounded in phase space, exhibit extreme sensitivity to initial conditions. Consequently, when generating such trajectories numerically on the computer, the inaccuracies caused by the small numerical errors (due to discretization and finite-precision arithmetic) at every step, grow exponentially in time, thereby leading to very large errors in relatively short times. This effect calls into question the very relevance of numerically generated solutions of such systems. In some cases, however, it is possible to demonstrate that although the numerically generated trajectory diverges rapidly from the true (noiseless) trajectory, there exists a certain true trajectory *corresponding to a slightly different initial condition*, that *shadows*, i.e., remains close (step by step) to, the numerically generated trajectory for all time [1,2]. This property lends credence to computer-generated results. It has been shown, for example, that all hyperbolic systems are shadowable [3,4]. Even for systems that are unshadowable, it is often possible to demonstrate *finite-time shadowing*. For such systems, although it may not be typically possible to find a true trajectory that remains close to the numerically generated trajectory for *all* time, it may still be possible to divide the numerical trajectory into sections of finite duration, separated by *glitches*, such that each section is shadowed by some true trajectory (also of finite duration). If the time intervals between consecutive glitches is sufficiently long, then such finite time shadowing may still be useful for practical purposes.

In many situations, it is desirable to determine the shadowing orbit numerically [5,6]. For example, when trying to model a chaotic, physical system for which certain observed time series data are available, a convincing test of any candidate model would be whether there exist trajectories in the model system that shadow all typical trajectories experimentally observed in the physical system. An algorithm that generates shadowing orbits may prove invaluable in such situations.

Another application of recent interest is in the field of communication using chaos [7–16]. In such a situation, the transmitter and the receiver are usually identical chaotic systems. A signal sent from the transmitter to the receiver is employed to synchronize the receiver to the transmitter [11,17–31]. Only then can the message of interest be recovered. The quality of message recovery is typically limited both by the quality of the signal received and by the method of synchronization used. A noisy receiver orbit usually leads to noisy message recovery. An algorithm that finds shadowing orbits numerically may be used in these cases to find the *true* orbit corresponding to the noisy receiver orbit, which is, presumably, the transmitter orbit. The message of interest may then be recovered easily. Thus finding a shadowing trajectory effectively achieves noise reduction in such chaos-based communication systems [32–34].

II. NUMERICAL SHADOWING PROBLEM

The problem addressed in this paper is as follows. There exists a chaotic, dynamical system $\mathcal{S}$. If $\vec{X}_i$ represents its time-i state vector, then its evolution may be described as $\vec{X}_i = M(\vec{X}_{i-1})$, where M is some mixing, chaotic map [37] with just one Lyapunov exponent positive, and the rest negative [38]. There exists a T-long numerical orbit

*Electronic address: dutta@math.unh.edu

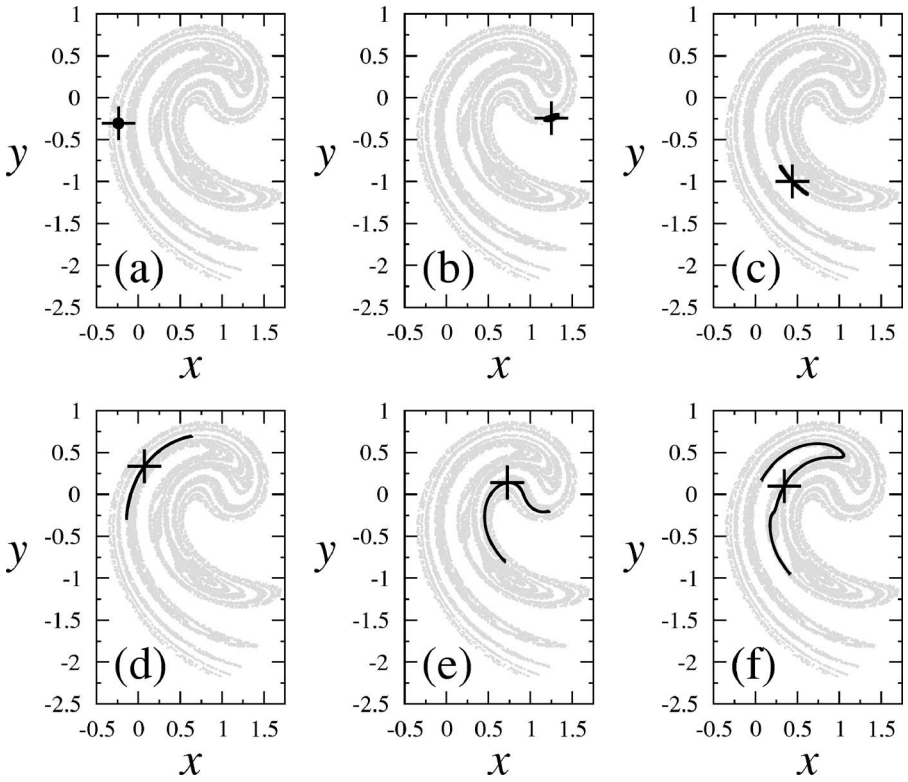

FIG. 1. The evolution of an ϵ disk of initial conditions $\mathcal{B}$ centered at the point $\vec{P}$ on the attractor $\mathcal{A}$, corresponding to the Ikeda map with $a=1$, $b=0.9$, $\kappa=0.4$, and $\eta=6.0$. This map has only one positive Lyapunov exponent and no zero Lyapunov exponents. The + symbol represents $\vec{P}$ and its images. The background shows the chaotic attractor $\mathcal{A}$.

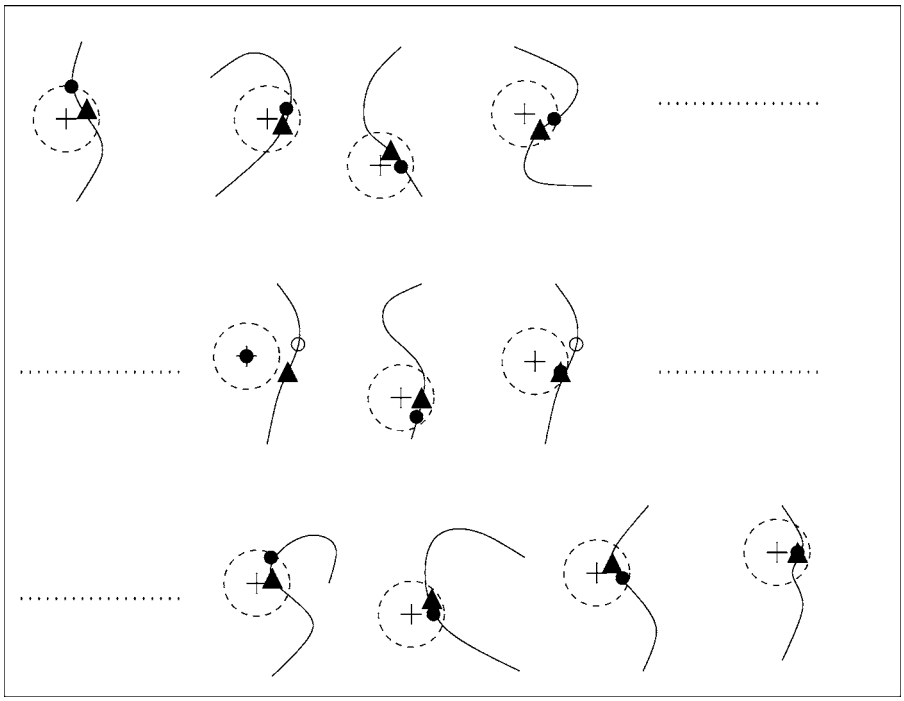

FIG. 2. Illustration of the synchronize-and-pullback algorithm. The + symbol represents the $\vec{W}_i$ points corresponding to the noisy $\vec{W}$ orbit. The dotted line represents the ϵ balls centered at the $\vec{W}_i$ points within which the shadowing solution is sought. The solid lines represent the local, unstable manifolds $\mathcal{L}_i$. The triangles represent the $\vec{Y}_i$ points, the empty circles represent the $\vec{Z}_i'$ points, and the solid circles represent the $\vec{Z}_i$ points. Notice how, at the very last iterate, the solid circle coincides with the triangle. At the preceding iterates, the solid circles coincide with the empty circles when the latter lie within the ϵ balls. If the empty circles lie outside the ϵ balls but the triangles lie within, then the solid circles coincide with the triangles. Otherwise, the solid circles coincide with the + symbols.

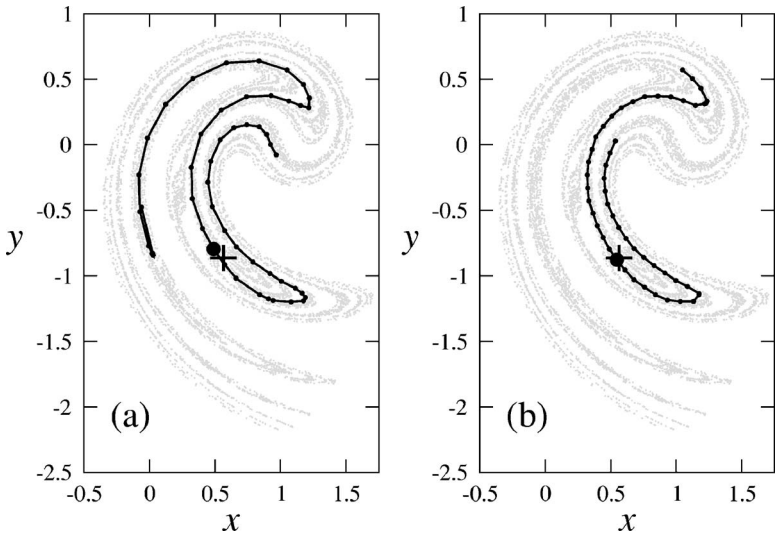

FIG. 3. Illustration of a 50 segment, piecewise-linear approximation of the local, unstable manifold corresponding to the Ikeda map with $a=1$, $b=0.9$, $\kappa=0.4$, and $\eta=6.0$. (a) The + symbol represents $\vec{W}_i$, the large circle represents $M(\vec{Y}_{i-1})$, the solid line represents $M(\tilde{\mathcal{L}}_{i-1})$, and the small circles represent its vertices. The background shows the chaotic attractor $\mathcal{A}$. (b) The + symbol represents $\vec{W}_i$, the large circle represents $\vec{Y}_i$, the solid line represents $\tilde{\mathcal{L}}_i$, and the small circles represent its vertices. The background shows the chaotic attractor $\mathcal{A}$.

$\vec{W}_0$-$\vec{W}_1$-$\vec{W}_2$-$\cdots$-$\vec{W}_T$—henceforth referred to as the $\vec{W}$ orbit—that is *noisy* in the sense that the stepwise *dynamic error*, $\delta_i=\|\vec{W}_i-M(\vec{W}_{i-1})\|$, is appreciable. The objective is to find a true orbit $\vec{Z}_0$-$\vec{Z}_1$-$\vec{Z}_2$-$\cdots$-$\vec{Z}_T$—henceforth refered to as the $\vec{Z}$ orbit—that shadows the $\vec{W}$ orbit. That is, for all $i=0,1,\ldots T$, $\epsilon_i\equiv\|\vec{W}_i-\vec{Z}_i\|\leqslant\epsilon$, where ϵ is small. Given that the exercise is to be implemented on a digital computer with finite precision, it will not, in general, be possible to find a truly accurate $\vec{Z}$ orbit. Therefore a $\vec{Z}$ orbit will be deemed as an acceptable shadowing orbit if the dynamic error associated with it is typically no larger than the typical stepwise error associated with an iteration of M on the computer. When such a $\vec{Z}$ orbit that shadows the $\vec{W}$ orbit for its entire length cannot be found, a piecewise shadowing solution is found in the form of a $\vec{Z}$ orbit characterized by typically long stretches of small dynamic error, punctuated by short bursts of large dynamic error viz. glitches. Such piecewise shadowing solutions are expected for finite-time shadowable systems.

III. SYNCHRONIZE-AND-PULLBACK ALGORITHM

The method presented in this paper obtains the shadowing $\vec{Z}$ orbit from the noisy $\vec{W}$ orbit in two steps. First, a particular scheme of synchronization is used to obtain an intermediate $\vec{Y}$ orbit (also noisy) from the $\vec{W}$ orbit. Then, by a process we call *pullback*, the $\vec{Z}$ orbit is computed from the $\vec{Y}$ orbit. Therefore we call our method *synchronize and pullback* [30].

A. Local, unstable manifold

The synchronization scheme central to the shadowing algorithm presented in this paper is a variation of the *slide-and-match* algorithm presented in Refs. [30,31]. However, for the sake of completeness, the scheme is presented here in its entirety. The algorithm is predicated on an interesting property peculiar to the dynamical system $\mathcal{S}$, when M, the map governing its dynamics, is a chaotic map with just one Lyapunov exponent positive, and the rest negative. As a concrete example, let $\mathcal{S}$ be the Ikeda system [35]. Then the map M may be described as follows:

$$x_i = a + b[x_{i-1}\cos(\theta_{i-1}) - y_{i-1}\sin(\theta_{i-1})], \tag{1}$$

$$y_i = b[x_{i-1}\sin(\theta_{i-1}) + y_{i-1}\cos(\theta_{i-1})], \tag{2}$$

where $\theta_{i-1}=\kappa-\eta/(1+x_{i-1}^2+y_{i-1}^2)$ and $\vec{X}_i\equiv(x_i,y_i)^T$. We pick parameter values $a=1$, $b=0.9$, $\kappa=0.4$, and $\eta=6.0$. Let $\mathcal{A}$ represent the fractal attractor corresponding to M.

Now consider a small, circular disk of initial conditions $\mathcal{B}$ centered at some point $\vec{P}$ on the attractor $\mathcal{A}$. Since only one of the Lyapunov exponents of M is positive, and the rest are all negative, the images of $\mathcal{B}$ (under iteration by M) stretch along one direction only, while shrinking along all the others. After a sufficient number of iterates the image of $\mathcal{B}$ looks like an essentially one-dimensional curve $\mathcal{L}$ lying in $\mathcal{A}$, with the corresponding image of $\vec{P}$ contained within it. Figure 1 provides an illustration of the process. Although the presented example corresponds to the two-dimensional Ikeda system, the property holds true for higher dimensional chaotic systems as well, when $\mathcal{B}$ is a small ball rather than a disk, just as long as the map M has only one positive Lyapunov exponent, and the rest negative.

Under further iteration by M, the images of $\mathcal{L}$ continue to stretch and fold, eventually growing to cover the entire attractor $\mathcal{A}$. Therefore, at every iterate, the ends of the image of $\mathcal{L}$ are truncated so that they never grow beyond a preset length. Then, at some much later iterate i, $\mathcal{L}_i$ (the image of $\mathcal{L}$) is called the *local unstable manifold* at $\vec{X}_i$ (the time-i image of $\vec{P}$) corresponding to the essentially semi-infinite orbit $\cdots\vec{X}_{i-2}\vec{X}_{i-1}\vec{X}_i$ [39]. An interesting property of the dynamics near $\mathcal{L}_i$ is that under iteration by M, points close to it converge onto it, although they diverge from one another along $\mathcal{L}_i$.

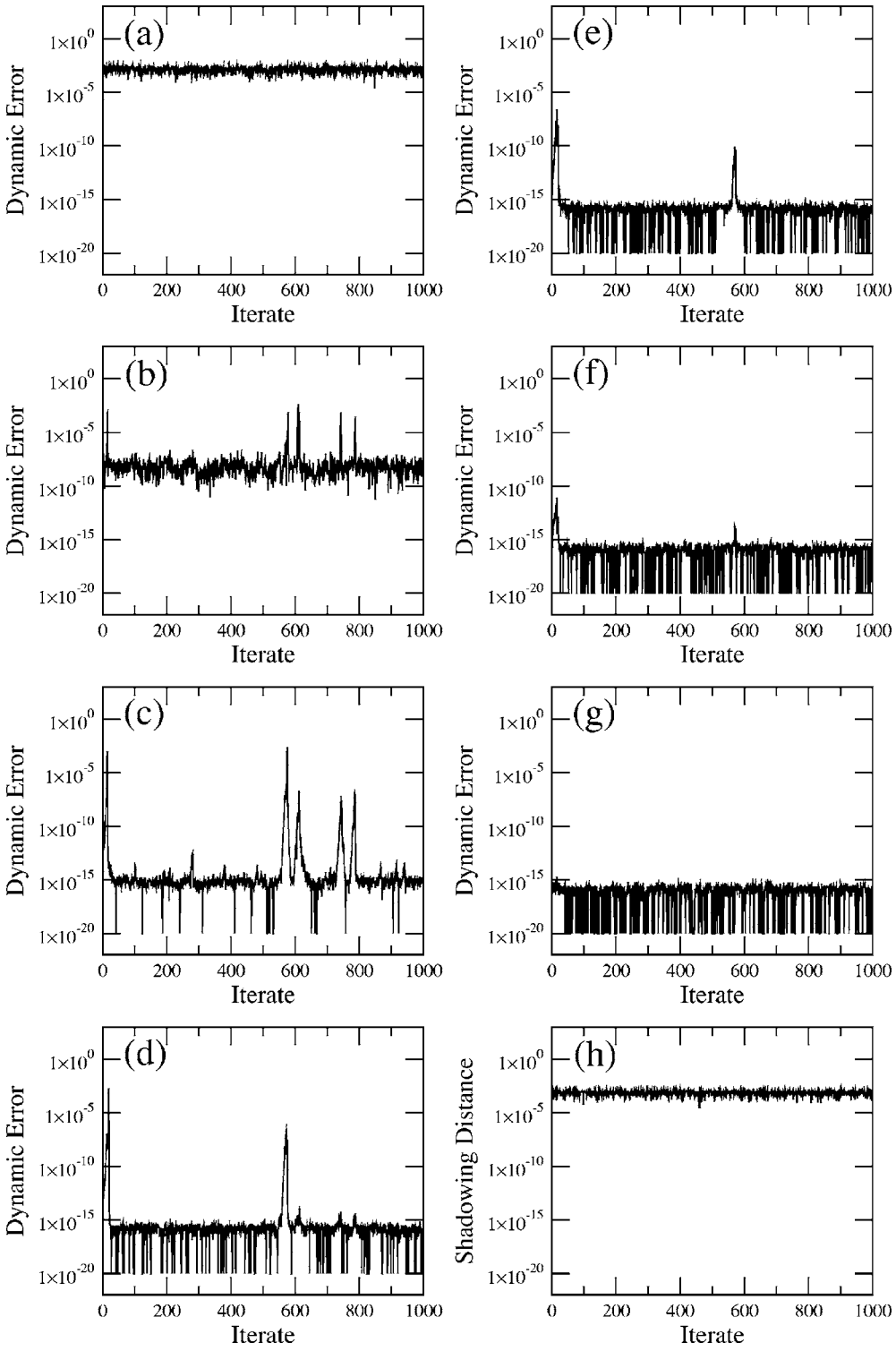

FIG. 4. For the Ikeda system with parameter values $a=1$, $b=0.9$, $\kappa=0.4$, and $\eta=6.0$, a noisy $\vec{W}$ orbit was generated using dynamical noise and observational noise of amplitudes 1×10^{-5} and 1×10^{-3}, respectively, along each axis. Several $\vec{Z}^{(k)}$ orbits were obtained by repeated synchronize-and-pullback refinement passes. (a) The stepwise dynamic error, $\|\vec{W}_i - M(\vec{W}_{i-1})\|$, vs the iterate i. (b) The stepwise dynamic error, $\|\vec{Z}_i^{(1)} - M(\vec{Z}_{i-1}^{(1)})\|$, vs the iterate i. (c) The stepwise dynamic error, $\|\vec{Z}_i^{(2)} - M(\vec{Z}_{i-1}^{(2)})\|$, vs the iterate i. (d) The stepwise dynamic error, $\|\vec{Z}_i^{(3)} - M(\vec{Z}_{i-1}^{(3)})\|$, vs the iterate i. (e) The stepwise dynamic error, $\|\vec{Z}_i^{(4)} - M(\vec{Z}_{i-1}^{(4)})\|$, vs the iterate i. (f) The stepwise dynamic error, $\|\vec{Z}_i^{(5)} - M(\vec{Z}_{i-1}^{(5)})\|$, vs the iterate i. (g) The final stepwise dynamic error, $\|\vec{Z}_i^{(6)} - M(\vec{Z}_{i-1}^{(6)})\|$, vs the iterate i. (h) The final stepwise shadowing distance, $\|\vec{Z}_i^{(6)} - \vec{W}_i\|$, vs the iterate i. Values lower than 1×10^{-20} have been plotted as 1×10^{-20}.

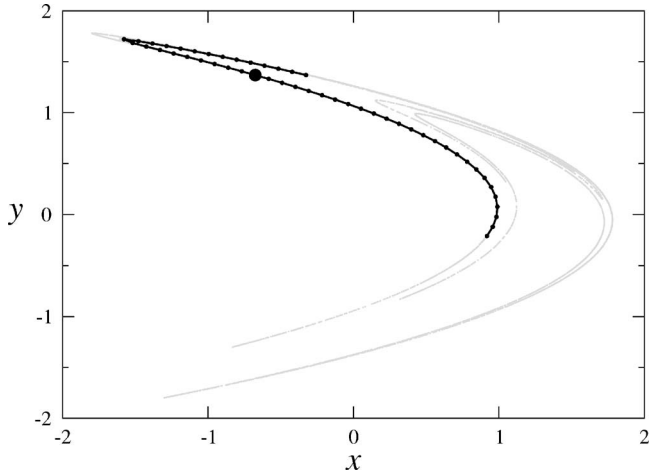

FIG. 5. Illustration of a 50 segment, piecewise-linear approximation of the local, unstable manifold corresponding to the Henon map with parameter values $a=1.4$ and $b=0.3$. The large circle represents $\vec{Y}_i$, the solid line represents $\tilde{\mathcal{L}}_i$, and the small circles represent its vertices. The background shows the chaotic attractor.

B. Synchronization: $\vec{W}$ orbit to $\vec{Y}$ orbit

The process of synchronization used to generate the $\vec{Y}$ orbit from the $\vec{W}$ orbit begins with the choice of $\vec{Y}_0$. For this, we must first decide upon a value for ϵ, the upper bound for the stepwise shadowing distance, $\epsilon_i \equiv \|\vec{W}_i - \vec{Z}_i\|$. Any point on the attractor $\mathcal{A}$ within a distance of ϵ from $\vec{W}_0$ may be chosen. Let $\mathcal{L}_0$ be the local, unstable manifold containing $\vec{Y}_0$. At all subsequent time steps, $\vec{Y}_i$ is chosen as that point on $M(\mathcal{L}_{i-1})$ that is closest to $\vec{W}_i$. And $\mathcal{L}_i$ is taken to be a subset of $M(\mathcal{L}_{i-1})$ containing $\vec{Y}_i$, with length no more than a preset limit. In some sense then, $\vec{Y}_i$ is obtained from $\vec{Y}_{i-1}$ by an iteration under M followed by an appropriate *slide* along $M(\mathcal{L}_{i-1})$.

C. Pullback: $\vec{Y}$ orbit to $\vec{Z}$ orbit

Although the $\vec{Y}$ orbit itself is not a true orbit, the manner in which it was generated allows us to find a true $\vec{Z}$ orbit that stays close to it at every step. We begin by identifying $\vec{Z}_T$ with $\vec{Y}_T$. Then, for every $i=0,1,\ldots,T-1$, we pick $\vec{Z}_i'$ as that point on $\mathcal{L}_i$ whose forward image is the closest to $\vec{Z}_{i+1}$. In fact, when $\vec{Z}_{i+1} \in \mathcal{L}_{i+1}$, it is possible to find a $\vec{Z}_i'$ whose forward image is actually $\vec{Z}_i$. This is because by construction $\mathcal{L}_{i+1} \subseteq M(\mathcal{L}_i)$, for all $i=0,1,\ldots,T-1$. Note that this does not require the map M to be invertible, since if $M(\vec{a})=\vec{b}$, then even if M is noninvertible, there typically exist neighborhoods $N_{\vec{a}}$ of $\vec{a}$ and $N_{\vec{b}}$ of $\vec{b}$ such that $M(N_{\vec{a}})=N_{\vec{b}}$, and each point of $N_{\vec{b}}$ has an inverse in $N_{\vec{a}}$ that is unique. If $\|\vec{Z}_i' - \vec{W}_i\| \leqslant \epsilon$, then $\vec{Z}_i'$ is picked as $\vec{Z}_i$. Otherwise, if $\|\vec{Y}_i - \vec{W}_i\| \leqslant \epsilon$, then $\vec{Y}_i$ is picked as $\vec{Z}_i$. Otherwise, $\vec{Z}_i$ is identified with $\vec{W}_i$. Figure 2 provides an illustration of this process of synchronization followed by pullback.

D. Approximating the local, unstable manifold

The crucial component in the successful implementation of the described algorithm is the accuracy of the local, unstable manifold approximation. Thus a numerical scheme that is both reliable and computationally efficient is called for. A relatively simple yet highly accurate method would be to approximate $\mathcal{L}_i$ by a *cloud* of points clustered around $\vec{Y}_i$. Under iteration by M, the images of these points tend to diverge. To preserve finiteness therefore the points lying far away from $\vec{Y}_i$ are deleted, while new points are added close to $\vec{Y}_i$ Although straightforward to implement, this approach is computationally very expensive. Another possible approach would be to simply approximate $\mathcal{L}_i$ by its tangent at $\vec{Y}_i$. While extremely efficient from a computational perspective, the quality of such an approximation would render it fragile under even very modest levels of noise.

As in Refs. [30,31], the time-i local, unstable manifold $\mathcal{L}_i$ is approximated in this paper by a piecewise-straight line with its middle vertex at $\vec{Y}_i$. Given that the quality of this approximation is central to the quality of the final shadowing, a few details about the method ought to be mentioned. For ease of discussion, let us use the symbol $\tilde{\mathcal{L}}_i$ to represent the piecewise-linear approximation to $\mathcal{L}_i$. In order to obtain $\tilde{\mathcal{L}}_i$ from $\tilde{\mathcal{L}}_{i-1}$, we first generate $M(\tilde{\mathcal{L}}_{i-1})$, the piecewise-straight line defined by the vertex points which are the images of the vertices of $\tilde{\mathcal{L}}_{i-1}$ under M. Clearly, $M(\tilde{\mathcal{L}}_{i-1})$ cannot be accepted as $\tilde{\mathcal{L}}_i$ without any modification, since such a process of evolution will quickly render any approximation invalid owing to the tendency of the unstable manifold to stretch and fold under evolution. Therefore we first determine $\vec{Y}_i$ as that point on $M(\tilde{\mathcal{L}}_{i-1})$ that is closest to $\vec{W}_i$. We then consider $\vec{Y}_i$ as the central vertex of $\tilde{\mathcal{L}}_i$. A quadratic spline is then passed through $\vec{Y}_i$ and the vertices of $M(\tilde{\mathcal{L}}_{i-1})$. The new vertices defining $\tilde{\mathcal{L}}_i$ are then chosen as points on the aforementioned spline, keeping the following points in mind:

(i) *No segment may be longer than a certain, preset maximum*. While almost any choice of a maximum allowed length for every segment will prevent the $\tilde{\mathcal{L}}_i$'s from growing beyond bound, a judicious choice is necessary in order to maintain the quality of the approximation. As long as the segments are not so short that the finite precision arithmetic of the computer is an issue, the shorter the segment lengths, the better is the quality of the approximation. In fact, to leading order, the approximation error is a quadratic function of the segment length.

(ii) *No two adjacent segments may form an angle smaller than a certain, preset value*. As mentioned earlier, the unstable manifold tends to both stretch and fold under evolution. While the previous precaution guards the $\tilde{\mathcal{L}}_i$'s from growing beyond bound, the precaution of imposing a lower bound on the angle between two adjacent segments prevents the $\tilde{\mathcal{L}}_i$'s from folding back upon themselves with segments overlapping one another.

(iii) *The total length of $\tilde{\mathcal{L}}_i$ must be sufficiently large compared to the distance between $\vec{Y}_i$ and $M(\vec{Y}_{i-1})$ along $M(\tilde{\mathcal{L}}_{i-1})$.*

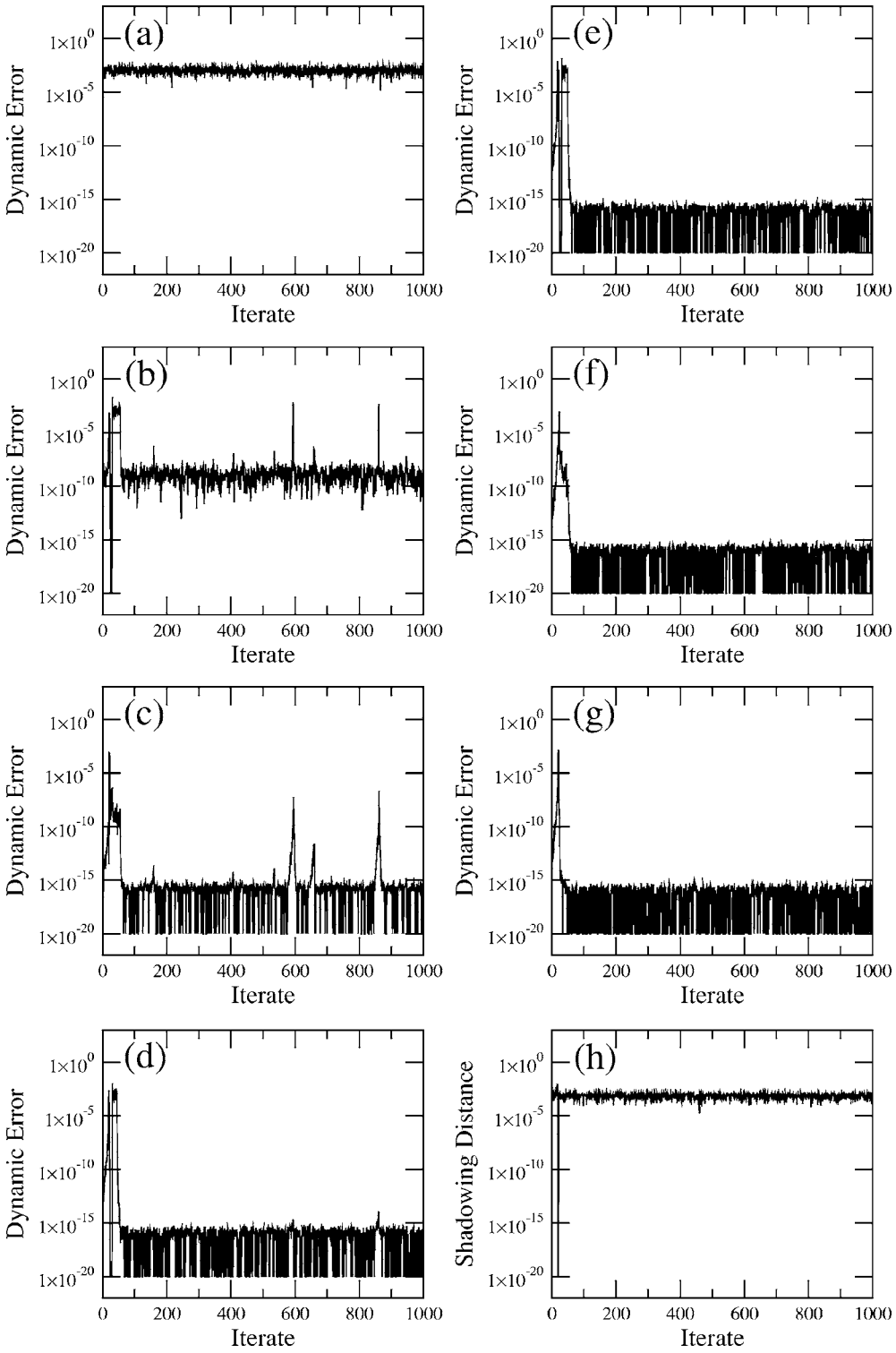

FIG. 6. For the Henon system with parameter values $a=1.4$ and $b=0.3$, a noisy $\vec{W}$ orbit was generated using dynamical noise and observational noise of amplitudes 1×10^{-5} and 1×10^{-3}, respectively, along each axis. Several $\vec{Z}^{(k)}$ orbits were obtained by repeated synchronize-and-pullback refinement passes. (a) The stepwise dynamic error, $\|\vec{W}_i - M(\vec{W}_{i-1})\|$, vs the iterate i. (b) The stepwise dynamic error, $\|\vec{Z}_i^{(1)} - M(\vec{Z}_{i-1}^{(1)})\|$, vs the iterate i. (c) The stepwise dynamic error, $\|\vec{Z}_i^{(2)} - M(\vec{Z}_{i-1}^{(2)})\|$, vs the iterate i. (d) The stepwise dynamic error, $\|\vec{Z}_i^{(3)} - M(\vec{Z}_{i-1}^{(3)})\|$, vs the iterate i. (e) The stepwise dynamic error, $\|\vec{Z}_i^{(4)} - M(\vec{Z}_{i-1}^{(4)})\|$, vs the iterate i. (f) The stepwise dynamic error, $\|\vec{Z}_i^{(5)} - M(\vec{Z}_{i-1}^{(5)})\|$, vs the iterate i. (g) The final stepwise dynamic error, $\|\vec{Z}_i^{(6)} - M(\vec{Z}_{i-1}^{(6)})\|$, vs the iterate i. (h) The final stepwise shadowing distance, $\|\vec{Z}_i^{(6)} - \vec{W}_i\|$, vs the iterate i. Values lower than 1×10^{-20} have been plotted as 1×10^{-20}.

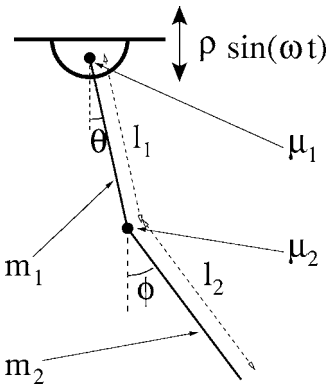

FIG. 7. The forced, damped, double pendulum.

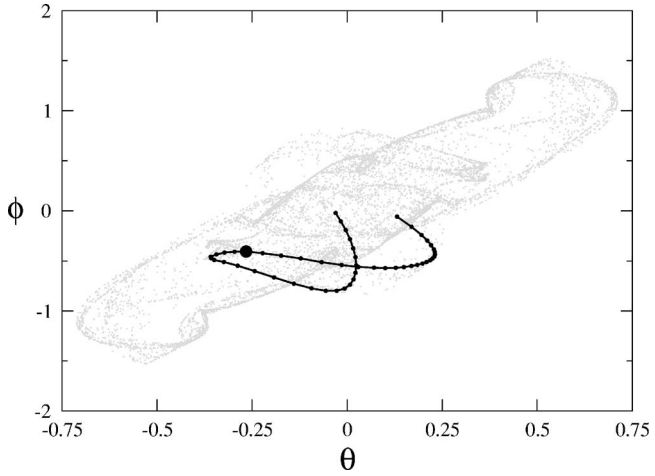

FIG. 8. Illustration of a 50 segment, piecewise-linear approximation of the local, unstable manifold corresponding to the Poincaré return map for the forced, damped, double pendulum with parameter values $l=1$, $m=0.5$, $\mu_1=0.25$, $\mu_2=0.125$, $\rho=0.375$, and $\omega=\pi$. The large circle represents $\vec{Y}_i$, the solid line represents $\tilde{\mathcal{L}}_i$, and the small circles represent its vertices. The background shows the chaotic attractor. While the true system is four dimensional, the figure shows a two-dimensional projection onto the $\theta-\phi$ plane. The angles θ and ϕ are plotted in radians.

This is clearly necessary in order for the $\tilde{\mathcal{L}}_i$'s to be useful for synchronization.

(iv) *The typical length of $\tilde{\mathcal{L}}_i$ should be based on the typical value of the distance between $\vec{Y}_i$ and $M(\vec{Y}_{i-1})$ along $M(\tilde{\mathcal{L}}_{i-1})$.* While we need the $\tilde{\mathcal{L}}_i$'s to be sufficiently longer than the distances between the $\vec{Y}_i$'s and the $M(\vec{Y}_{i-1})$'s along the $M(\tilde{\mathcal{L}}_{i-1})$'s, they should not be much longer. There are two reasons for this. First, the longer the $\tilde{\mathcal{L}}_i$'s, the longer will the individual segments be, thereby leading to reduced quality. Second, if any $\tilde{\mathcal{L}}_i$ is too long, then multiple folds of it may all come close to the corresponding $\vec{W}_i$. This increases the risk of picking an incorrect $\vec{Y}_i$, thereby causing an unnecessary glitch in the shadowing orbit.

When $\tilde{\mathcal{L}}_i$ is obtained from $\tilde{\mathcal{L}}_{i-1}$ in the manner outlined above, we call $\tilde{\mathcal{L}}_i$ the *normalized image* of $\tilde{\mathcal{L}}_{i-1}$.

In order to generate the $\vec{Y}$ orbit from the $\vec{W}$ orbit, we first pick any point $\vec{P}$ on the attractor $\mathcal{A}$. We then pick a set of $2N$ nearby points (not necessarily on $\mathcal{A}$) such that these $2N+1$ points (including $\vec{P}$) lie on a short, straight line segment with $\vec{P}$ in the center. Treating this as our very first $\tilde{\mathcal{L}}$, we evolve it along with $\vec{P}$ in the manner described previously. After a sufficient number of iterates, the normalized image of $\tilde{\mathcal{L}}$ converges to the local unstable manifold of the corresponding image of $\vec{P}$. The system is further evolved until $\tilde{\mathcal{L}}'$, the normalized image of $\tilde{\mathcal{L}}$, comes to within ϵ of $\vec{W}_0$. $\vec{Y}_0$ is then chosen as the point on $\tilde{\mathcal{L}}'$ that lies closest to $\vec{W}_0$. $\vec{Y}_0$ serves as the central vertex point for $\tilde{\mathcal{L}}_0$. The other $2N$ vertex points are then chosen in the manner described previously. Thus we obtain $\vec{Y}_0$ and $\tilde{\mathcal{L}}_0$, in order to begin the process of the generation of the $\vec{Y}$ orbit from the $\vec{W}$ orbit by synchronization. Figure 3 provides an illustration of this process of evolution of the $\tilde{\mathcal{L}}$'s.

E. Refinement

Had the true local, unstable manifolds, the $\mathcal{L}$'s, been available, the $\vec{Z}$ orbit obtained using the above-described algorithm would have been the desired "true" orbit that shadows the noisy $\vec{W}$ orbit. Since the $\tilde{\mathcal{L}}$'s are but approximations to the $\mathcal{L}$'s, errors are introduced into the $\vec{Z}$ orbit. Therefore the synchronize-and-pullback algorithm must be applied repeatedly in a process of successive refinement.

Let the notation, $\vec{Z}^{(k)}$ orbit, represent the $\vec{Z}$ orbit obtained after the kth refinement pass. The $\vec{Z}^{(0)}$ orbit may be identified with the $\vec{W}$ orbit. Then, at the kth refinement pass, the $\vec{Y}^{(k)}$ orbit is obtained by synchronization from the $\vec{Z}^{(k-1)}$ orbit as described in Sec III B (the $\vec{Z}^{(k-1)}$ orbit plays the role of the $\vec{W}$ orbit while the $\vec{Y}^{(k)}$ orbit plays the role of the $\vec{Y}$ orbit). The $\vec{Z}^{(k)}$ orbit is obtained subsequently from the $\vec{Y}^{(k)}$ orbit by the process of pullback as described in Sec. III C. The reason this process of successive refinement works is that our method of approximating the local, unstable manifolds is self-adjusting. As mentioned in Sec. III D, the typical length of the $\tilde{\mathcal{L}}$'s is based on the sliding adjustments along the $\tilde{\mathcal{L}}$'s required for the generation of the $\vec{Y}$ orbit. Now, after the very first refinement pass, the dynamic error associated with the $\vec{Z}^{(1)}$ orbit is significantly lower than that associated with the $\vec{Z}^{(0)}$ orbit (i.e., the $\vec{W}$ orbit). Therefore, at the second refinement pass, the sliding adjustments required to generate the $\vec{Y}^{(2)}$ orbit are smaller than the corresponding adjustments at the first refinement pass. Consequently, the typical length of the $\tilde{\mathcal{L}}^{(2)}$'s is smaller than that of the $\tilde{\mathcal{L}}^{(1)}$'s. Since the number of segments used for the $\tilde{\mathcal{L}}$'s is always the same, a smaller length for the $\tilde{\mathcal{L}}^{(2)}$'s implies a smaller length for the individual segments that compose the $\tilde{\mathcal{L}}^{(2)}$'s. Given that the $\tilde{\mathcal{L}}$'s are piecewise linear approximations to the $\mathcal{L}$'s, the approximation errors must, to leading order, scale as the squares of

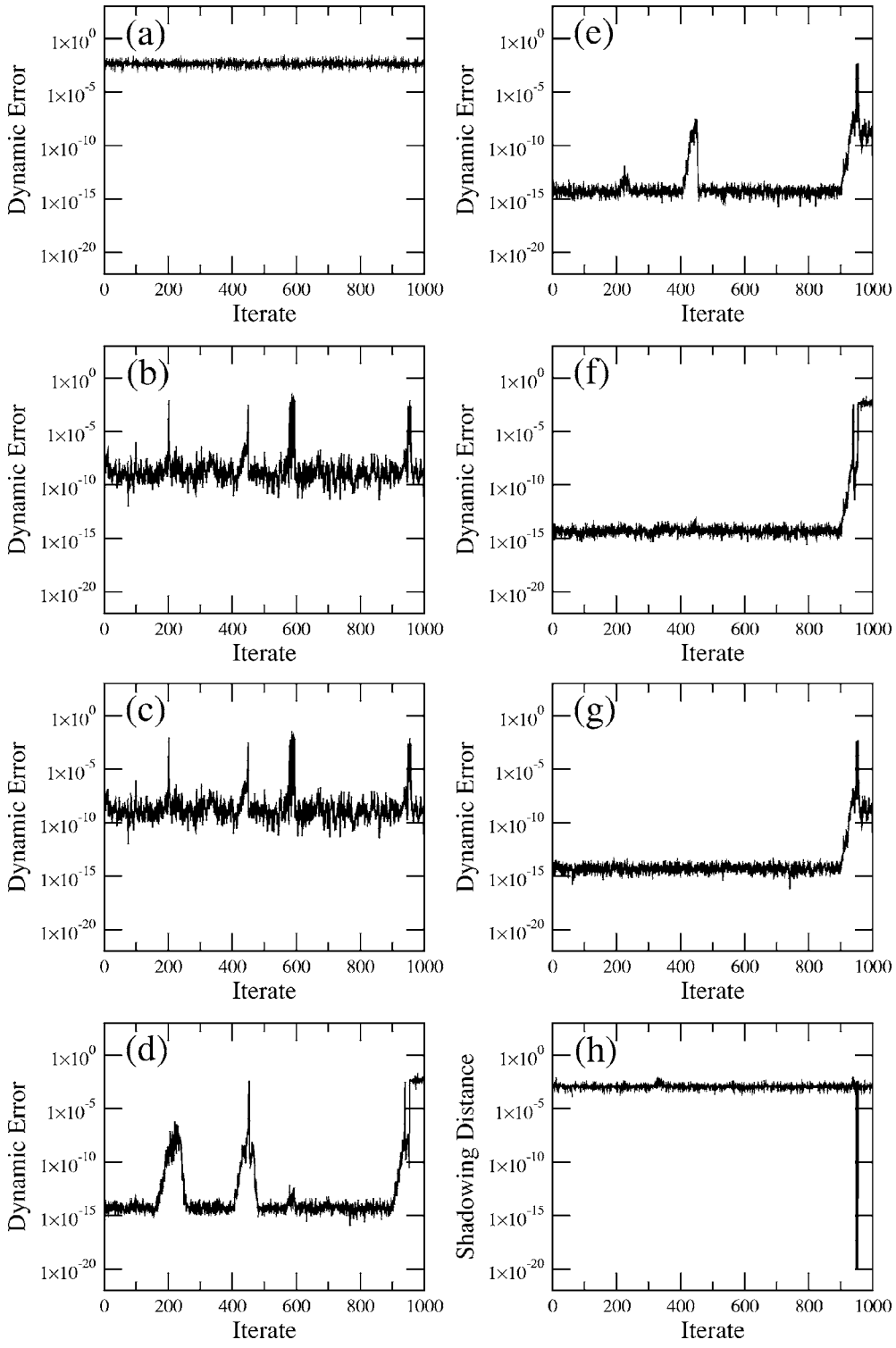

FIG. 9. For the forced, damped, double pendulum with parameter values $l=1$, $m=0.5$, $\mu_1=0.25$, $\mu_2=0.125$, $\rho=0.375$, and $\omega=\pi$, a noisy $\vec{W}$ orbit was generated using dynamical noise and observational noise of amplitudes 1×10^{-5} and 1×10^{-3}, respectively, along each axis. Several $\vec{Z}^{(k)}$ orbits were obtained by repeated synchronize-and-pullback refinement passes. (a) The stepwise dynamic error, $\|\vec{W}_i-M(\vec{W}_{i-1})\|$, vs the iterate i. (b) The stepwise dynamic error, $\|\vec{Z}_i^{(1)}-M(\vec{Z}_{i-1}^{(1)})\|$, vs the iterate i. (c) The stepwise dynamic error, $\|\vec{Z}_i^{(2)}-M(\vec{Z}_{i-1}^{(2)})\|$, vs the iterate i. (d) The stepwise dynamic error, $\|\vec{Z}_i^{(3)}-M(\vec{Z}_{i-1}^{(3)})\|$, vs the iterate i. (e) The stepwise dynamic error, $\|\vec{Z}_i^{(4)}-M(\vec{Z}_{i-1}^{(4)})\|$, vs the iterate i. (f) The stepwise dynamic error, $\|\vec{Z}_i^{(5)}-M(\vec{Z}_{i-1}^{(5)})\|$, vs the iterate i. (g) The final stepwise dynamic error, $\|\vec{Z}_i^{(6)}-M(\vec{Z}_{i-1}^{(6)})\|$, vs the iterate i. (h) The final stepwise shadowing distance, $\|\vec{Z}_i^{(6)}-\vec{W}_i\|$, vs the iterate i. Values lower than 1×10^{-20} have been plotted as 1×10^{-20}.

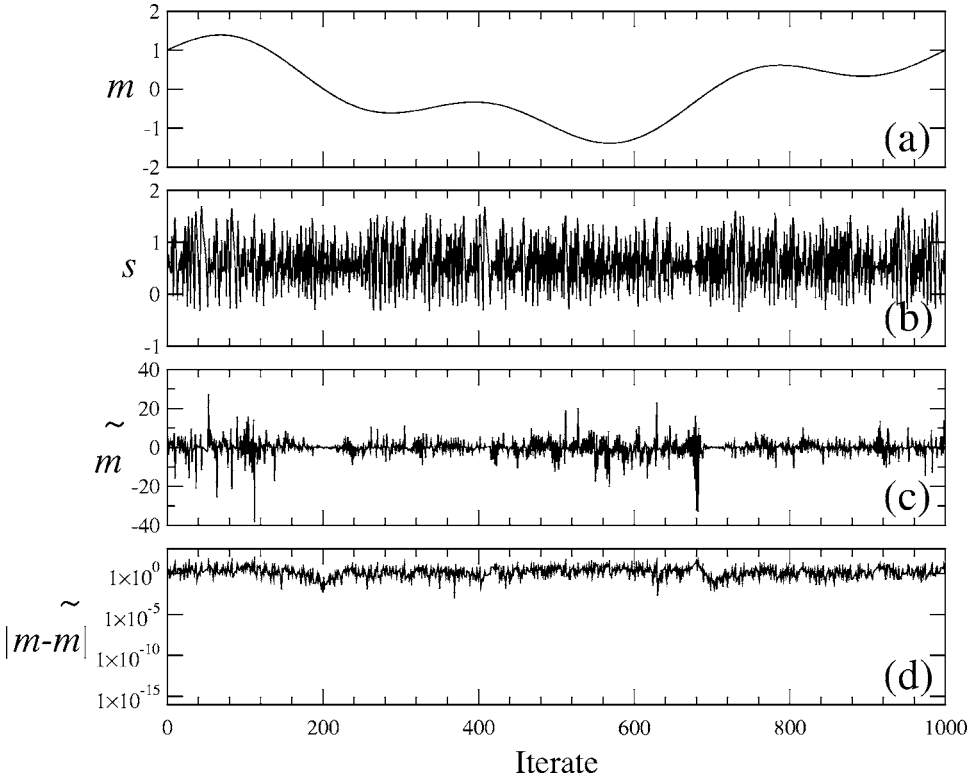

FIG. 10. Communication by synchronization of Ikeda maps: (a) The message stream m_i plotted as a function of the iterate i. (b) The signal stream s_i, plotted as a function of the iterate i. (c) The recovered message stream $\tilde{m}_i$, plotted as a function of the iterate i. (d) The message recovery error, $|\tilde{m}_i - m_i|$, plotted as a function of the iterate i.

the lengths of the individual segments. Therefore the dynamic error associated with the $\vec{Z}^{(2)}$ orbit obtained by pullback from the $\vec{Y}^{(2)}$ orbit must be much smaller than the dynamic error associated with the $\vec{Z}^{(1)}$ orbit. Thus, with every refinement pass, the dynamic error in the $\vec{Z}$ orbit decreases until it reaches the limit imposed by the machine precision. There may be short transients of higher error both at the beginning and at the end of the computed $\vec{Z}$ orbit. The process of generating the $\vec{Y}$ orbit from the $\vec{W}$ orbit contributes to the former transient, while the latter transient is related to the process of generating the $\vec{Z}$ orbit from the $\vec{Y}$ orbit.

IV. EXAMPLES OF NUMERICAL SHADOWING

Three numerical experiments were conducted to demonstrate the shadowing algorithm proposed in this paper. Results from those experiments are presented here as examples. All three examples share a common format. The noisy $\vec{W}$ orbits span 1001 iterates (corresponding to $T=1000$), and were generated using both dynamical noise and observational noise. Thus:

$$\vec{X}_i = M(\vec{X}_{i-1}) + \vec{\eta}_i^D, \tag{3}$$

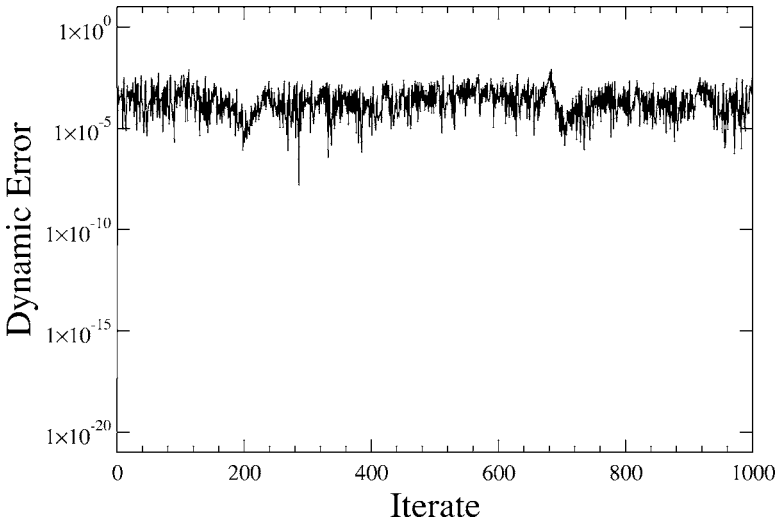

FIG. 11. The dynamic error corresponding to the $\vec{X}^{\mathcal{R}}$ orbit, $\|\vec{X}_i^{\mathcal{R}} - M(\vec{X}_{i-1}^{\mathcal{R}})\|$, plotted as a function of the iterate i.

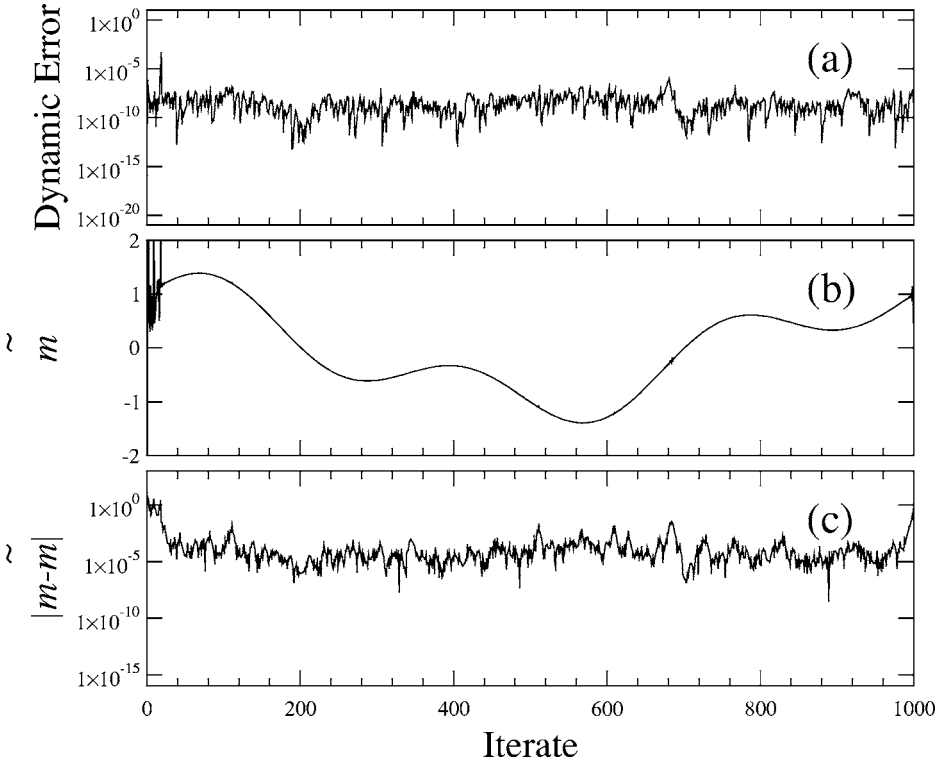

FIG. 12. Results after one synchronize-and-pullback refinement pass. (a) The dynamic error corresponding to the $\vec{Z}^{(1)}$ orbit, obtained after cleaning the $\vec{X}^{\mathcal{R}}$ orbit with a single refinement pass, plotted as a function of the iterate i. (b) $\tilde{m}_i^{(1)}$, the cleaned, recovered message corresponding to the $\vec{Z}^{(1)}$ orbit, plotted as a function of the iterate i. (c) The corresponding message recovery error, $|\tilde{m}_i^{(1)} - m_i|$, plotted as a function of the iterate i.

$$\vec{W}_i = \vec{X}_i + \vec{\eta}_i^O. \tag{4}$$

Equation (3) holds for all $i=1$–1000 while Eq. (4) holds for all $i=0$–1000. $\vec{X}_0$ was chosen to be a point on the attractor $\mathcal{A}$, corresponding to the chaotic map M. $\vec{\eta}_i^D$ and $\vec{\eta}_i^O$ represent the dynamical noise and the observational noise, respectively. $\vec{\eta}_i^D$ is a vector of random numbers with a uniform distribution in a cube of side 2×10^{-5} while $\vec{\eta}_i^O$ is a similar vector with a uniform distribution in a cube of side 2×10^{-3}. The synchronize-and-pullback procedure was then repeatedly applied to the $\vec{W}$ orbits thereby generating a sequence of $\vec{Z}$ orbits in a process of successive refinement.

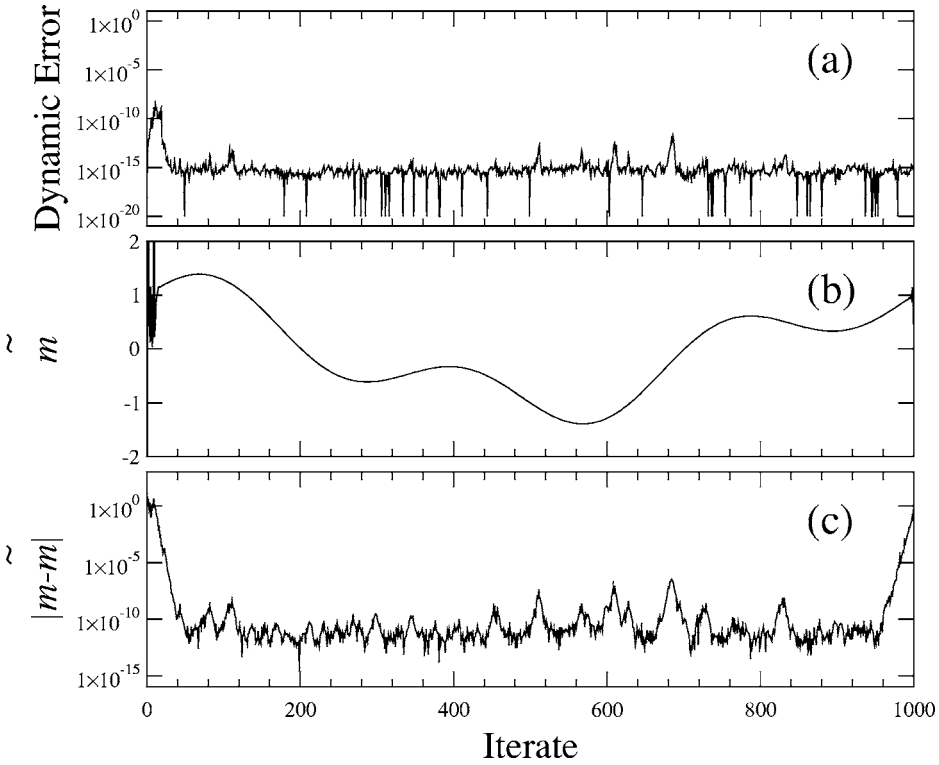

FIG. 13. Results after two synchronize-and-pullback refinement passes. (a) The dynamic error corresponding to the $\vec{Z}^{(2)}$ orbit, obtained after cleaning the $\vec{X}^{\mathcal{R}}$ orbit with two refinement passes, plotted as a function of the iterate i. (b) $\tilde{m}_i^{(2)}$, the cleaned, recovered message corresponding to the $\vec{Z}^{(2)}$ orbit, plotted as a function of the iterate i. (c) The corresponding message recovery error, $|\tilde{m}_i^{(2)} - m_i|$, plotted as a function of the iterate i.

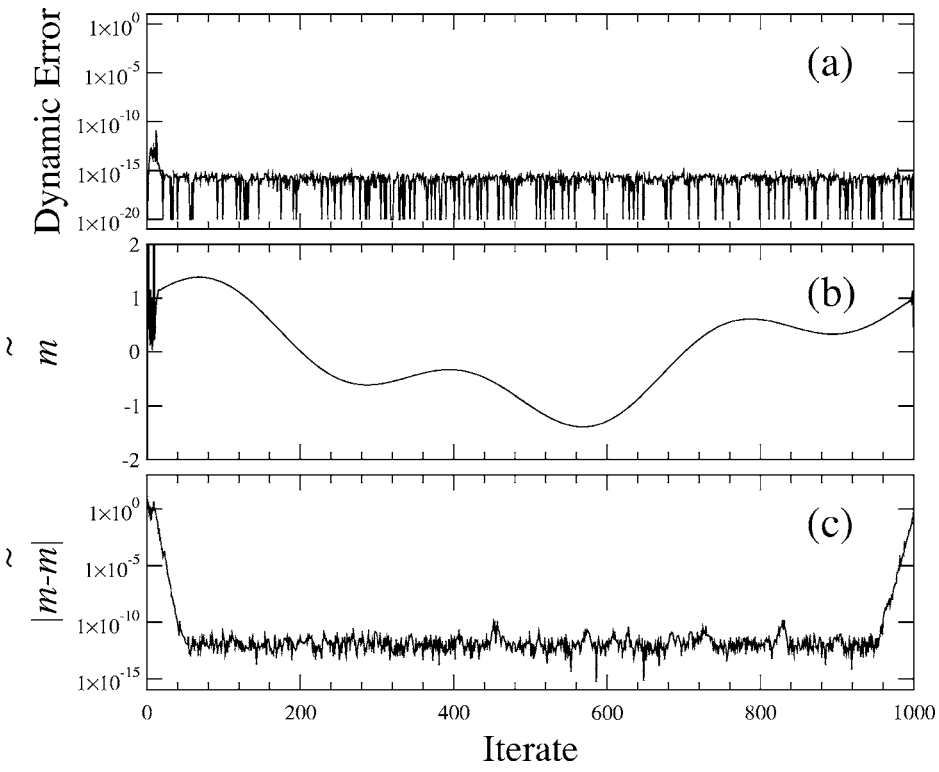

FIG. 14. Results after three synchronize-and-pullback refinement passes. (a) The dynamic error corresponding to the $\vec{Z}^{(3)}$ orbit, obtained after cleaning the $\vec{X}^{\mathcal{R}}$ orbit with three refinement passes, plotted as a function of the iterate i. (b) $\tilde{m}_i^{(3)}$, the cleaned, recovered message corresponding to the $\vec{Z}^{(3)}$ orbit, plotted as a function of the iterate i. (c) The corresponding message recovery error, $|\tilde{m}_i^{(3)}-m_i|$, plotted as a function of the iterate i.

A. Ikeda map

The first example involves the Ikeda system. The map M, in this case, is defined by Eqs. (1) and (2). We pick parameter values $a=1$, $b=0.9$, $\kappa=0.4$, and $\eta=6.0$. Figure 3 shows the corresponding chaotic attractor, as well as a piecewise-linear approximation of a typical, local, unstable manifold. A noisy $\vec{W}$ orbit was generated in the manner described before using dynamical noise and observational noise of amplitudes 1×10^{-5} and 1×10^{-3}, respectively, along each axis. Figure 4 shows the stepwise dynamic error, $\|\vec{Z}_i^{(k)}-M(\vec{Z}_{i-1}^{(k)})\|$, corresponding to the $\vec{Z}^{(k)}$ orbits obtained by the repeated application of the synchronize-and-pullback procedure. As shown in Fig. 4(g), at the end of the sixth refinement pass, the stepwise dynamic error is down to the typical stepwise error associated with the evolution of the Ikeda system on the computer. At the same time, the corresponding stepwise shadowing distances shown in Fig. 4(h) are of the order of 1×10^{-3}, as should be expected given the noise levels used in generating the $\vec{W}$ orbit. Thus the $\vec{Z}^{(6)}$ orbit meets the requirements for an acceptable shadowing orbit.

B. Henon map

The second example involves the Henon system [36]. The map M, in this case, is defined by the following equations:

$$x_i = a - x_{i-1}^2 + by_{i-1}, \tag{5}$$

$$y_i = x_{i-1}. \tag{6}$$

We pick parameter values $a=1.4$ and $b=0.3$. Figure 5 shows the corresponding chaotic attractor, as well as a piecewise-linear approximation of a typical, local, unstable manifold. A noisy $\vec{W}$ orbit was generated in the manner described before using dynamical noise and observational noise of amplitudes 1×10^{-5} and 1×10^{-3} respectively, along each axis. Figure 6 shows the stepwise dynamic error, $\|\vec{Z}_i^{(k)}-M(\vec{Z}_{i-1}^{(k)})\|$, corresponding to the $\vec{Z}^{(k)}$ orbits obtained by the repeated application of the synchronize-and-pullback procedure. As shown in Fig. 6(g), at the end of the sixth refinement pass, except for a short initial transient, the stepwise dynamic error is down to the typical stepwise error associated with the evolution of the Henon system on the computer. At the same time, the corresponding stepwise shadowing distances shown in Fig. 6(h), are of the order of 1×10^{-3}, as should be expected given the noise levels used in generating the $\vec{W}$ orbit. Thus the $\vec{Z}^{(6)}$ orbit meets the requirements for an acceptable shadowing orbit.

C. Forced, damped, double pendulum

The third example involves the forced, damped, double pendulum. As described in Refs. [30,31], this is a mechanical device consisting of a uniform rod suspended by a hinge from a second rod which is, in turn, suspended from a support by a second hinge (see Fig. 7). The rods (pendula) are free to swing in a vertical plane. θ and ϕ represent the deviations of the inner and the outer pendula from the vertical, while m_1, m_2 and l_1, l_2 represent their masses and lengths, respectively. Viscous dissipation is provided by linear friction at the hinges with μ_1 and μ_2 as the coefficients of friction (viscosity). An external forcing mechanism vertically oscillates the top support sinusoidally with amplitude ρ and frequency ω. Without loss of generality, we set

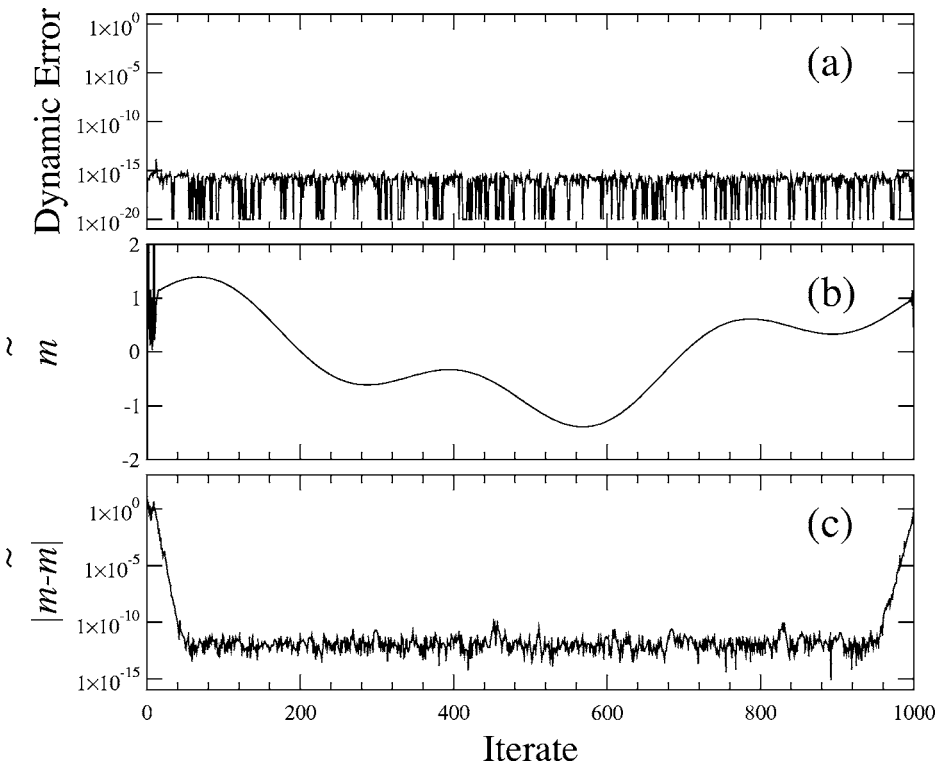

FIG. 15. Results after four synchronize-and-pullback refinement passes. (a) The dynamic error corresponding to the $\vec{Z}^{(4)}$ orbit, obtained after cleaning the $\vec{X}^{\mathcal{R}}$ orbit with four refinement passes, plotted as a function of the iterate i. (b) $\tilde{m}_i^{(4)}$, the cleaned, recovered message corresponding to the $\vec{Z}^{(4)}$ orbit, plotted as a function of the iterate i. (c) The corresponding message recovery error, $|\tilde{m}_i^{(4)}-m_i|$, plotted as a function of the iterate i.

$m_1=l_1=g=1$ (g is the acceleration due to gravity), and drop the subscripts from m_2 and l_2 to obtain

$$\dot{\theta}=u, \tag{7}$$

$$\dot{\phi}=v, \tag{8}$$

$$\dot{u}=\frac{1}{D}\left[\left(\frac{l^2}{6}\right)F_1-\left(\frac{ml\cos(\theta-\phi)}{4}\right)F_2\right], \tag{9}$$

$$\dot{v}=\frac{1}{D}\left[\left(\frac{-l\cos(\theta-\phi)}{4}\right)F_1+\left(\frac{3m+1}{6}\right)F_2\right], \tag{10}$$

where

$$F_1=-mlv^2\sin(\theta-\phi)-\tilde{g}(2m+1)\sin(\theta)-2\mu_1 u+2\mu_2(v-u), \tag{11}$$

$$F_2=lu^2\sin(\theta-\phi)-\tilde{g}l\sin(\phi)-2\mu_2(v-u)/m, \tag{12}$$

$$D=l^2(3m+1)/9-ml^2\cos(\theta-\phi)^2/4, \tag{13}$$

$$\tilde{g}=1-\rho\omega^2\sin(\omega t). \tag{14}$$

The time-$(2\pi/\omega)$ strobed Poincaré section reduces this five-dimensional system to a map with a four-dimensional state vector $\vec{X}\equiv(\theta,\phi,u,v)$, where all the quantities are measured at the beginning of every forcing cycle. We pick parameter values $l=1$, $m=0.5$, $\mu_1=0.25$, $\mu_2=0.125$, $\rho=0.375$, and $\omega=\pi$. The corresponding chaotic attractor and the piecewise linear approximation to a typical, local unstable manifold are shown in Fig. 8.

A noisy $\vec{W}$ orbit was generated in the manner described before using dynamical noise and observational noise of amplitudes 1×10^{-5} and 1×10^{-3}, respectively, along each axis. Figure 9 shows the stepwise dynamic error, $\|\vec{Z}_i^{(k)}-M(\vec{Z}_{i-1}^{(k)})\|$, corresponding to the $\vec{Z}^{(k)}$ orbits obtained by the repeated application of the synchronize-and-pullback procedure. As shown in Fig. 9(g), at the end of the sixth refinement pass, except for a short transient at the very end, the stepwise dynamic error is down to the typical stepwise error associated with the evolution of the forced, damped, double pendulum system on the computer. At the same time, the corresponding stepwise shadowing distances shown in Fig. 9(h) are of the order of 1×10^{-3}, as should be expected given the noise levels used in generating the $\vec{W}$ orbit. Thus the $\vec{Z}^{(6)}$ orbit meets the requirements for an acceptable shadowing orbit.

V. NOISE FILTRATION IN CHAOTIC COMMUNICATION

It was mentioned earlier that finding shadowing solutions to chaotic orbits has applications in the context of noise filtration in chaotic communications. A concrete example is provided in this section as demonstration.

Many methods exist in the literature that achieve communication using the synchronization of chaotic systems [7–16]. The basic idea behind the method adopted here is as follows. There is a system $\mathcal{S}$, whose dynamics is governed by a chaotic map M. For concreteness, we pick $\mathcal{S}$ to be the Ikeda system described previously. We have two identical copies of $\mathcal{S}$ that we call $\mathcal{T}$ (for *transmitter*) and $\mathcal{R}$ (for *receiver*) whose state vectors are represented by $\vec{X}_i^{\mathcal{T}}\equiv(x_i^{\mathcal{T}},y_i^{\mathcal{T}})^T$ and $\vec{X}_i^{\mathcal{R}}\equiv(x_i^{\mathcal{R}},y_i^{\mathcal{R}})^T$, respectively. System $\mathcal{T}$ is allowed to evolve

without any perturbation. The values of its x component $x_i^{\mathcal{T}}$ are transmitted to $\mathcal{R}$ after superimposing a scaled-down, low amplitude version of the message stream m_i. The receiver $\mathcal{R}$ uses this incoming signal s_i to synchronize (approximately) itself to $\mathcal{T}$ by the method of direct substitution. The difference between $x_i^{\mathcal{T}}$ and s_i, after appropriate scaling, is the recovered message stream $\tilde{m}_i$. The set of equations describing the entire process follows:

$$\theta_{i-1}^{\mathcal{T}} = \kappa - \eta/(1 + {x_{i-1}^{\mathcal{T}}}^2 + {y_{i-1}^{\mathcal{T}}}^2), \tag{15}$$

$$x_i^{\mathcal{T}} = a + b[x_{i-1}^{\mathcal{T}} \cos(\theta_{i-1}^{\mathcal{T}}) - y_{i-1}^{\mathcal{T}} \sin(\theta_{i-1}^{\mathcal{T}})], \tag{16}$$

$$y_i^{\mathcal{T}} = b[x_{i-1}^{\mathcal{T}} \sin(\theta_{i-1}^{\mathcal{T}}) + y_{i-1}^{\mathcal{T}} \cos(\theta_{i-1}^{\mathcal{T}})], \tag{17}$$

$$s_i = x_i^{\mathcal{T}} + \rho \times m_i, \tag{18}$$

$$\theta_{i-1}^{\mathcal{R}} = \kappa - \eta/(1 + s_{i-1}^2 + {y_{i-1}^{\mathcal{R}}}^2), \tag{19}$$

$$x_i^{\mathcal{R}} = a + b[s_{i-1} \cos(\theta_{i-1}^{\mathcal{R}}) - y_{i-1}^{\mathcal{R}} \sin(\theta_{i-1}^{\mathcal{R}})], \tag{20}$$

$$y_i^{\mathcal{R}} = b[s_{i-1} \sin(\theta_{i-1}^{\mathcal{R}}) + y_{i-1}^{\mathcal{R}} \cos(\theta_{i-1}^{\mathcal{R}})], \tag{21}$$

$$\tilde{m}_i = (s_i - x_i^{\mathcal{R}})/\rho. \tag{22}$$

A numerical experiment was performed using $\rho = 0.0001$ and the rest of the parameter values as in Sec. III A: $a = 1$, $b = 0.9$, $\kappa = 0.4$, and $\eta = 6.0$. The results of the numerical experiment are illustrated in Fig. 10. The performance is evidently rather poor. In fact, the typical magnitude of the message recovery error, $\tilde{m}_i - m_i$, is an order of magnitude greater than the typical magnitude of the message of interest, thus rendering the message undecipherable.

The situation may be improved dramatically by the use of shadowing. According to the notation used so far in this paper, the $\vec{X}^{\mathcal{R}}$ orbit followed by the receiver $\mathcal{R}$ is regarded as the $\vec{W}$ orbit. Figure 11 shows the dynamic error associated with this $\vec{X}^{\mathcal{R}}$ orbit. This orbit is then "cleaned" using synchronize-and-pullback refinement passes. It is hoped that, at least for small ρ, the sequence of $\vec{Z}^{(k)}$ orbits converges to the original $\vec{X}^{\mathcal{T}}$ orbit. Hence the corresponding $\tilde{m}_i^{(k)}$'s must converge to the authentic m_i as well [40]. This process of noise filtration by shadowing is illustrated in Figs. 12–15. By the conclusion of the fourth refinement pass, the message recovery error, except for short transients at the beginning and at the end, is down to the limits imposed by machine precision. Thus the noise is effectively filtered.

It may appear that the entire recovered message stream $\tilde{m}_i$ must be available before the shadowing-based, noise filtration algorithm described here can be applied. This would appear to reduce the appeal of the method in situations where real-time, noise filtration is necessary. However, this is not necessary. An inspection of Fig. 15 will reveal that the transient at the end is approximately 50 segments long (in fact, the slope of the logarithm of the filtered message recovery error as a function of the iterate is roughly equal to the positive Lyapunov exponent associated with the chaotic map). Therefore only a few *future* iterates are necessary in order for the algorithm to work. Thus in a situation where real time filtration is necessary, the shadowing-based method presented here may still be used to provide a filtered message stream in real time, albeit with a short delay.

VI. CONCLUSION

The primary advantage of the synchronize-and-pullback method for computing shadowing orbits is that irrespective of the system dimension, it reduces the computing of shadowing orbits to an essentially one-dimensional problem, as long as the dynamics is described by a chaotic map with a single positive Lyapunov exponent, and all the other Lyapunov exponents negative. This is a significant simplification for high-dimensional systems. Second, unlike several shadowing algorithms in the literature [5,6], the synchronize-and-pullback method does not require the map M to be invertible. Third, since the local, unstable manifold was approximated by a piecewise-linear curve of positive length, rather than by a tangent vector, the method works for higher levels of noise than linear methods. Furthermore, the quality of this approximation is directly related to the number of segments used. Thus, depending on the computational resources available, the effectiveness of the algorithm is adjustable.

Summing up, a different method with several interesting advantages has been presented that generates high-quality shadowing orbits for noisy orbits corresponding to chaotic maps with a single, positive Lyapunov exponent (and the rest of the exponents negative). It is expected that the method may be extended to systems described by chaotic maps with multiple, positive Lyapunov exponents. For such systems, the computational complexity of our shadowing algorithm is expected to depend only on the number of positive Lyapunov exponents rather than on the total system dimension. Unfortunately, an effective numerical approximation for a multidimensional manifold is complicated, and the programming effort involved is considerable. Extending the synchronize-and-pullback method to such cases of chaotic maps with multiple, positive Lyapunov exponents will be the subject of future work.

[1] B. Lani-Wayda, *Hyperbolic Sets, Shadowing and Persistence for Noninvertible Mappings in Banach Spaces* (Longman Group Ltd., Harlow, Essex, 1995).

[2] S. Y. Pilyugin, *Shadowing in Dynamical Systems* (Springer, New York, 1999).

[3] D. V. Anosov, Proc. Steklov Inst. Math. **90**, 1 (1967).

[4] R. Bowen, J. Diff. Eqns. **18**, 333 (1975).

[5] C. Grebogi, S. M. Hammel, J. A. Yorke, and T. Sauer, Phys.

Rev. Lett. **65**, 1527 (1990).
[6] S. Dawson, C. Grebogi, T. Sauer, and J. A. Yorke, Phys. Rev. Lett. **73**, 1927 (1994).
[7] S. Hayes, C. Grebogi, and E. Ott, Phys. Rev. Lett. **70**, 3031 (1993).
[8] S. Hayes, C. Grebogi, E. Ott, and A. Mark, Phys. Rev. Lett. **73**, 1781 (1994).
[9] K. M. Cuomo and A. V. Oppenheim, Phys. Rev. Lett. **71**, 65 (1993).
[10] L. Kocarev, K. S. Halle, K. Eckert, L. O. Chua, and U. Parlitz, Int. J. Bifurcation Chaos Appl. Sci. Eng. **2** 709 (1992).
[11] L. Kocarev and U. Parlitz, Phys. Rev. Lett. **74**, 5028 (1995).
[12] Y.-C. Lai, E. Bollt, and C. Grebogi, Phys. Lett. A **255**, 75 (1999).
[13] M. Hasler, Int. J. Bifurcation Chaos Appl. Sci. Eng. **8**, 647 (1998).
[14] T. L. Carroll, Phys. Rev. E **67**, 026207 (2003).
[15] A. Uchida, M. Kawano, and S. Yoshimori, Phys. Rev. E **68**, 056207 (2003).
[16] R. Mislovaty, E. Klein, I. Kanter, and W. Kinzel, Phys. Rev. Lett. **91**, 118701 (2003).
[17] H. Fujisaka and T. Yamada, Prog. Theor. Phys. **69**, 32 (1983).
[18] L. M. Pecora and T. L. Carroll, Phys. Rev. Lett. **64**, 821 (1990).
[19] C. W. Wu and L. O. Chua, Int. J. Bifurcation Chaos Appl. Sci. Eng. **3**, 1619 (1993).
[20] U. Parlitz, L. Kocarev, T. Stojanovski, and H. Preckel, Phys. Rev. E **53**, 4351 (1996).
[21] L. Kocarev, U. Parlitz, and T. Stojanovski, Phys. Lett. A **217**, 280 (1996).
[22] S. Fahy and D. R. Hamann, Phys. Rev. Lett. **69**, 761 (1992).
[23] R. E. Amritkar and N. Gupte, Phys. Rev. E **47**, 3889 (1993).
[24] T. Stojanovski, L. Kocarev, and U. Parlitz, Phys. Rev. E **54**, 2128 (1996).
[25] M. Ding and E. Ott, Phys. Rev. E **49**, R945 (1994).
[26] L. Junge and U. Parlitz, Phys. Rev. E **64**, 055204(R) (2001).
[27] E. E. N. Macau, C. Grebogi, and Y.-C. Lai, Phys. Rev. E **65**, 027202 (2002).
[28] P. So, E. Ott, and W. P. Dayawansa, Phys. Lett. A **176**, 421 (1993).
[29] P. So, E. Ott, and W. P. Dayawansa, Phys. Rev. E **49**, 2650 (1994).
[30] M. Dutta, Ph.D. thesis, University of Maryland, College Park, 2000.
[31] M. Dutta, Phys. Rev. E **72**, 026217 (2005).
[32] S. Hammel, Phys. Lett. A **148**, 421 (1990).
[33] J. D. Farmer and J. J. Sidorowich, Physica D **47**, 373 (1991).
[34] M. Davies, Physica D **79**, 174 (1994).
[35] E. Ott, *Chaos in Dynamical Systems* (Cambridge University Press, Cambridge, U.K., 1993), p. 278.
[36] E. Ott, *Chaos in Dynamical Systems* (Ref. [35]) p. 13.
[37] We assume that our chaotic system is "mixing" in the limited sense that for any point $\vec{P}$ in the attractor, the trajectories corresponding to any two typical initial conditions occasionally come very close to $\vec{P}$ simultaneously.
[38] It is expected that the proposed algorithm may be extended to include maps with multiple positive Lyapunov exponents as well as flows, but the software effort required to implement this numerically is daunting, and will be the subject of future work.
[39] The local unstable manifold thus defined may exist even when the map M is noninvertible. For a rigorous definition, see Ref. [31].
[40] There are a few subtleties associated with this convergence that ought to be mentioned. First, the shadowing orbit need not be unique. More importantly, the chaotic system in question may not even be shadowable. However, as mentioned earlier in this paper, even for unshadowable systems, it is often possible to find finite-time shadowing solutions separated by glitches. When the dynamic noise in the $\vec{X}^{\mathcal{R}}$ orbit is small (this is ensured for small ρ), it is reasonable to expect at least finite-time shadowing solutions, with long intervals between glitches. Thus as long as ρ is small, the message stream m_i ought to be recoverable in general, interrupted by rare, short bursts.